total force on a bubble for Re = 311. Therefore, for freely rising air bubbles in water, $\mathbf{F}_B$ is usually neglected.

When the expressions for each component of $\mathbf{F}_p$ are introduced in [46], without considering Faxen and Basset forces, the equation of motion can be rearranged to look like

$$V_b(\rho_b + \rho_l C_M)\frac{d\mathbf{v}}{dt} = V_b \rho_l (1 + C_M)\frac{D\mathbf{u}}{Dt} + V_b(\rho_b - \rho_l)\mathbf{g} + \frac{1}{2}C_D \rho_l A_b \|\mathbf{U}_r\|\mathbf{U}_r + V_b \rho_l C_L (\mathbf{U}_r \times \boldsymbol{\omega}) \quad [48]$$

where the subscripts b and l are associated to the bubble and liquid, respectively. C_M, C_D, and C_L, are the added mass, drag and lift coefficients, respectively. V and A are the volume and projected area of the bubble, ρ the density, and $\mathbf{U}_r$ the relative velocity between the two phases given by [41]. Using the current notation, $\mathbf{U}_r$ is given by

$$\mathbf{U}_r = \mathbf{u} - \mathbf{v}, \quad [49]$$

and

$$\boldsymbol{\omega} = \nabla \times \mathbf{u}. \quad [50]$$

The components of $\boldsymbol{\omega}$ are given by [24]. The substantial acceleration of the liquid, the relative velocity and the cross product in the lift force are all evaluated at the center of the bubble (as if the bubble was not there).

6.1.3. Nature of the forces acting on the bubble

The left-hand side of [48] represents the bubble mass plus the liquid added mass times the bubble acceleration. On the right hand side appears firstly the force resulting from the pressure gradient and the shear stress of the liquid, when the bubble is not in the liquid. Next, it's the buoyancy force; then, the drag force; and finally, the lift force.

The virtual or mass force is an unsteady force due to the acceleration of the relative velocity between the bubble and the liquid. It is the force needed to accelerate the bubble surrounding

liquid. The liquid acceleration is produced by work done due to bubble/liquid interaction. The added mass coefficient C_M has a value of 0.5 for spherical particles, according to potential flow theory. However, C_M is actually a tensor called added mass matrix, or induced inertia tensor (Brennen 1995). The elements of the added mass matrix are determined from steady potential flows and/or the steady translation movement of the particle in the fluid. For spheres, the added mass matrix contains non-zero values only across the diagonal. These values equal 0.5 only for spheres embedded in infinite media. For non-spherical particles, however, all the elements of the added mass tensor are non-zero. This implies that the amount of liquid mass displaced depends on the shape of the bubble, as it is expected. For an ellipsoid, for example, the values depend on the aspect ratio of the ellipsoid.

For particles moving in non-linear trajectories in unsteady flows, a correction to C_M is introduced through the acceleration parameter (Crowe *et al.* 1998), or acceleration number (Michealides 1997), or acceleration modulus (Clift *et al.* 1978), Ac, which is defined by

$$\mathrm{Ac} = \frac{\|\mathbf{U}_r\|^2}{d_e \left\| \frac{d\,\mathbf{U}_r}{d\,t} \right\|}. \qquad [51]$$

The corrected value of C_M is given by (Michealides 1997)

$$C_M = 1.05 - \frac{0.066}{0.12 + \mathrm{Ac}^2}. \qquad [52]$$

Observe that as Ac tends to zero, C_M tends to 0.5. Recent results from numerical simulations indicate, however, that C_M equals 0.5 for spherical particles for a wide range of Re and Ac (Magnaudet 1997). Also, other experimental results have proven that C_M still is close to 0.5 even for distorted bubbles. Therefore, $C_M = 0.5$ is widely used in bubbly flow analysis.

The drag force is one of the well studied forces acting on any kind of fluid particle. The drag coefficient C_D is accurately calculated through empirical correlations, which only depend on Re (Clift *et al.* 1978; Fan & Tsuchiya 1990). These correlations, however, yield average values, which can be far from the actual instantaneous values, because of unsteadiness of the flow, the

oscillation of the particle projected area, and/or the particle's acceleration. In fact, the average C_D is usually determined through the expression for the drag force in [48] assuming that the particle already travels at terminal velocity without the presence of lateral (lift) forces. Therefore, the magnitude of the drag force equals the buoyancy force value. Results have shown that depending on the average operation used to analyze the experimental data, C_D can be considerably different (Hunt *et al.* 1992).

Another problem regarding C_D is the contamination of the systems in which the particle flows. For air bubble of about 2 to 4 mm d_e rising in water, for example, the terminal velocity is reduced in contaminated systems, and the drag coefficient is increased. This *contaminated* C_D is actually closer to the C_D of a rigid particle at the same Re, and usually is calculated through the correlation for rigid particles. The contamination of the bubble surface brings out other phenomena that complicate the analysis of the flow field. As the surface of the bubble gets contaminated it affects its surface tension, σ, and the shear stress, then the internal circulation is suppressed. There is an enhancement of boundary layer separation, and then vortex shedding. As mentioned above, wall influence on the drag coefficient is introduced by the empirical wall factor λ.

The lift force is the most difficult one to measure or compute. This is so because it is generally smaller that the other interacting forces. Its importance comes from the role it can play on bubble migration, and then phase distribution, because it is normal to the direction of motion of the particle. According to Batchelor (1967), the lift force arises due to the vorticity generation at a rigid surface. As mentioned above, bubbles moving in liquids with non-high purity behave close to a rigid particle. The vorticity can also be generated because of shear in the liquid. Further, the liquid velocity gradient may induce a rotation of the bubble. The uneven pressure distribution surrounding the rocking bubble yields a lateral force on the bubble. This force is called Saffman lift force. For some authors, however, the lift force arises from the Saffman effect only when there is no particle rotation. Even if the bubble would not rotate, the pressure field can induce lateral movement to the bubble. This Saffman force, without rotation, usually appears in the equation of motion as the only component of the total lift force. This is the case shown in [48] for the lift force.

The Magnus effect is the lift force due to the rotation of the particle. In this case the lateral force arises from the pressure difference between the sides of the particle. This is due to the different velocities at each side, generated by the rotation. The particle may be spinning because

of collisions with other particles or the wall. Rotation also may be induced by the shear in the liquid flow. The Magnus effect is rarely included in the equation of motion of the particles because there is no information available about the rotation of the particles. An expression for this force is given by (Crowe *et al.* 1998)

$$\mathbf{F}_{\mathbf{Mag}} = \frac{1}{2}\rho_l \|\mathbf{U}_\mathbf{r}\| C_{\mathrm{LR}} A_b \left(\frac{\mathbf{U}_\mathbf{r} \times \boldsymbol{\omega}_\mathbf{r}}{\left\| \boldsymbol{\Omega} - \frac{1}{2}\boldsymbol{\omega} \right\|} \right), \qquad [53]$$

where C_{LR} is the rotational lift coefficient and $\boldsymbol{\omega}_\mathbf{r}$ is the difference between the angular velocity of the particle $\boldsymbol{\Omega}$, and half the liquid vorticity $\boldsymbol{\omega}$, that is

$$\boldsymbol{\omega}_\mathbf{r} = \boldsymbol{\Omega} - \frac{1}{2}\boldsymbol{\omega}. \qquad [54]$$

$\boldsymbol{\omega}_\mathbf{r}$ can be considered as the relative rotation motion of the particle with respect to the fluid.

It should be noted that the lift coefficient C_{L} in [48] is only due to shear, and has been called the pure straining lift coefficient C_{LS} (Magnaudet 1997). The total lift coefficient C_{L} is the sum of C_{LS} and C_{LR}, and then the total lift force is the sum of the contribution from the flow shear plus the rotation of the particle. For large Re, $C_{\mathrm{L}} = 0.5$, obtained from potential inviscid flow, is widely used. When one of the lift forces is not considered in the equation of motion, the lift coefficient of the other force is assumed to equal C_{L}. As pointed out by Crowe *et al.* (1998), C_{L} remains unclear for intermediate Re.

Finally, the buoyancy force is due to the density difference between the bubble and the liquid.

6.2. Accuracy of measurements

The uncertainties in determining both the shape and the forces acting on the bubble come from the accuracy of the DGHT algorithm presented in Chapter IV. The value obtained for the error was 0.08 mm (3 pixel), and it corresponded to the measurements in the X-direction (the images from the center camera). This value is the error associated to the value each of the

semiaxes a, b, and c, and also for the centroid of the bubbles.

Following the error analysis presented in Chapter V, the maximum errors of the velocity components of the bubble are 4.8 mm/s, and consequently 288.0 mm/s^2 for the acceleration components. The errors of the acceleration of the liquid, calculated from the velocity components given in Chapter V, are 94.8 mm/s^2 in the X-direction, 346.2 mm/s^2 in the Y-direction, and 83.4 mm/s^2 in the Z-direction. Although these values are of the order of the velocity and acceleration of the bubble, it should be noted that the bubble travels at an order of magnitude faster.

To determine the error associated to the calculation of the forces acting on the bubble, and consequently on the calculations of C_D and C_L, [48] can be casted as

$$V_b \rho_l \left[\frac{\rho_b}{\rho_l} \frac{d\mathbf{v}}{dt} + C_M \left(\frac{d\mathbf{v}}{dt} - \frac{D\mathbf{u}}{Dt} \right) - \frac{D\mathbf{u}}{Dt} \right] = V_b (\rho_b - \rho_l)\mathbf{g} + \left[\frac{1}{2} C_D \rho_l A_b \|\mathbf{U_r}\| \mathbf{U_r} \right]_{\Uparrow} + \left[\frac{1}{2} C_L \rho_l A_b \|\mathbf{U_r}\| \mathbf{U_r} \right]_{\perp} \quad [55]$$

The left hand side represents the total inertia of the system. On the right hand side the expression for the lift force in [48] has been changed to the common expression used in aerodynamics for the total lift. This expression allows for an easier calculation of the lift coefficient. The parallel and perpendicular symbols are introduced to stress that the drag force acts parallel to $\mathbf{U_r}$, while the lift is normal to it.

The maximum error on the calculation of the inertia force comes from the y-components of the acceleration terms. By combining the error from both the bubble and the liquid accelerations, by using [25], the error in the Y-direction is 450.3 mm/s^2. The error in the X-direction is 303.2 mm/s^2; and 299.8 mm/s^2 for the Z-direction. The error in the calculation of the bubble is about 0.4 mm^3.

The substantial accelerations above are easily computed in a Lagrangian reference frame. This is an advantage of the particle tracking techniques. This also justifies the need of a hybrid tracking technique in these situations. The ART2 NN tracked the seed particles during 4 consecutive frames, which is the same number of frames in which the bubble appeared in the viewing volume, in general. Therefore, the Lagrangian approach can be used for both the liquid

and the bubble simultaneously.

6.3. Experimental results and discussion

In this experiment 81 bubbles were released, one at a time, in quiescent water, in a 12.7 mm i.d. pipe. The time interval between each release was of few minutes. It is known that it takes less than a second for the disturbances generated by the bubble to vanish, so the flow was totally stagnant when the next bubble was released. Each camera captured the image of the bubble only for 3, or 4, or in very rare events 5 frames, out of the total 27 frames for each bubble release. In general, the bubble could be seen in 4 frames; however, only three frames from the Center and Shadow cameras could be used for the 3D reconstruction method shown in Chapter IV. The following results are those from bubbles that could be three-dimensionally reconstructed.

Following the nodalization scheme for the bubble presented in Chapter V (figure 17a), the data were divided according to the bubble trajectory. In this case a similar trajectory is specified for the bubbles which rose up in similar fashion at least two consecutive frames out of the three frames. Although this condition seems too weak for the motion of the bubbles in the test volume, it should be considered that the lateral motion of the bubbles was nicely continuous. That is, when a bubble moved from a region into other, the distance traveled was small and the trajectory was smooth enough that the bubble was considered to be rising in a similar trajectory. On the other hand, if a bubble moved in different regions and did not satisfy the condition of staying at least two consecutive time steps in one of the nodal zones, then it did not belong to the same trajectory. Also, bubbles crossing more than two boundaries during its rising path were not part of a similar trajectory.

Few bubbles traveled in regions 2 and 3 (see figure 16) so they were not considered for the data analysis. The final trajectory distributions considered for data analysis were: 24 bubbles traveled through trajectory 111; 18 bubbles rose up in trajectory 444; and 15 bubbles followed trajectory 555. Combinations of all trajectories, and for those close to the wall were also included in the averaging operations. The combination of all trajectories (111, 444, and 555) is referred to as trajectory *all*, while the combination of trajectories close to the wall (444 and 555) is denoted as trajectory *out*.

6.3.1. Bubble shape and velocity analysis

The Reynolds number of the bubbles, Re_b, was in the range from 350 to 700. At this range, a

Table 2. Bubble dimensions

Bubble Trajectory	a and σ_a [mm]	b and σ_b [mm]	c and σ_c [mm]	d and σ_d [mm]
111	1.24	1.46	1.34	2.69
	0.10	0.08	0.07	0.12
444	1.26	1.43	1.36	2.70
	0.10	0.09	0.07	0.13
555	1.27	1.45	1.38	2.73
	0.09	0.09	0.09	0.13
out	1.27	1.44	1.37	2.71
	0.09	0.09	0.08	0.13
all	1.25	1.45	1.36	2.70
	0.10	0.08	0.08	0.13

bubble freely rising in stagnant water presents oscillations in shape and rising path. The predicted shape is ellipsoidal, although not necessarily symmetric. The motion is expected to be helical and/or zigzag, and even a rocking motion. The ellipsoidal shape, however, would be observed in systems with high-purity working fluids, and with negligible wall influence. Clift *et al.* (1978) considered that for $0.12 < \lambda < 0.6$, and $Re_b > 100$, walls can cause elongation of bubbles in the vertical direction, so for the ellipsoidal shape, the result would tend to change to spheroidal shape again.

At least 3 images of a bubble need to be three-dimensionally reconstructed in order to calculate the three components of the acceleration vector. The acceleration was assigned to the second of the 3D reconstructions of a bubble (the one in the middle). Such second reconstruction corresponded in 93% of the experiment to the third frame (t_p = 33.33 ms), in which the bubble appeared in the test volume. Table 2 shows the average and standard deviation from the mean for each different trajectory, and combinations of trajectories, of the values of the semiaxes and spherical equivalent diameter determined from the instantaneous reconstructions.

From Table 2, it can be concluded that the shape of the bubbles was oblate spheroid. The minimum and maximum eccentricity were $e = b / c = 1.05$ for trajectory 555, and $e = b / a = 1.18$ for trajectory 111, respectively. Observe that the largest dimension was always in the Y-direction (b in here), followed by the semiaxis in the Z-direction (c), and the smallest semiaxis was in the X-direction (a). From Table 2, the wall effect factor was $\lambda = 0.21$, and $Re_b > 100$ in all cases, so the wall influence could be noticed. Since all bubbles were of the same size, approximately, it was not possible to determine the role of the volume on the rise path. It is well known that bubbles of less than 3 mm in diameter tend to collect close to the wall. In this experiment almost all bubbles were smaller than 3 mm of d_e, and the trajectories were 42% along the pipe core, so no tendency was observed for this experiment condition.

Another feature to note is that bubbles rising along the pipe center had a maximum value of the semimajor axis, while the bubbles rising close to the wall had larger semiaxes in the X and Z directions. This is in agreement with the fact that the wall influence is to elongate the dimensions of the semiaxes parallel to the wall, while it diminishes the dimension of the semiaxis perpendicular to the wall. The maximum error for any value in Table 2 is 6.5%, and it corresponds to the average value of a for trajectory 111 (0.08/1.24). Because of the magnitude of this error, the wall influence results presented are still tendencies (clear tendencies though). It will be necessary to reduce the error to 1 pixel (0.03 mm) to draw definite conclusions. It should be noted that the standard deviations σ of each parameter in Table 2 are not their associated errors, but only the spread of data from the calculated mean value shown. The actual errors were presented in the previous section.

In the present study, the bubbles rose in a helical path.. Actually, the prediction for rising path is based on direct experimental observations. The rocking motion was also observed, with both the PIV and shadow cameras, as shown in figures 18 and 19. Figures 18 and 19 are typical samples of shapes and trajectories found in the measurements, so they can be used as examples. The ellipsoidal shape of a bubble is the result of the pressure difference inside and on the surface of the bubble. This pressure difference increases with higher Re_b. During a PIV measurement, seed particles are needed to track the liquid motion; and therefore the system is contaminated. Contaminants can induce changes in the physical properties of the fluids, and/or can agglomerate on the bubble surface. It is known that contaminants tend to harden the bubble interface, tending to make the bubble to act as a rigid particle. Thus the bubble is not allowed to laterally expand.

For a bubble rising in a helical or zigzag path, the frequency of contact with the wall is high, when the radius of the spiral trajectory that the bubble would follow in an infinite medium is larger than the radius of the pipe in which it actually is moving. The collision induces a decrease in the lateral dimensions, and an increase in the vertical ones. Therefore, by combining the effects of the contaminants and the collision frequency with the pipe wall, the final shape should be closer to a spheroid (an oblate spheroid actually) than to an ellipsoid. This was the case, as deduced from figures 18 and 19, and the data shown in Table 2.

Another way to study bubble shape and trajectory is through the dimensionless numbers associated to the bubble. Grace (1973) and Bhaga & Weber (1981) have presented maps of shape regimes for single bubbles rising in Newtonian liquids based on Re_b, M, and Eo. The maps, however, excluded any data where wall influence could be noticed. The map of the regimes given by Grace (1973) predicts a transition between spherical to ellipsoidal bubbles for Re_b = 350, and from ellipsoidal to wobbling for Re_b = 700. Table 3 shows the average and standard deviations of the dimensionless numbers Re_b, M, and Eo associated to the second reconstructed bubble, and the bubble speed. The value of the velocity is the magnitude of the three-dimensional velocity vector, which was used to compute the dimensionless numbers. It is important to address the shape of a fluid particle which allows for physical analysis of the forces acting on the bubble. This is due to that Re_b is the ratio of magnitude of the inertial forces to the viscous forces. M only involves physical properties of the system under study, so it is commonly used as a parameter, which for the air-water system is $M = 2.56\times10^{-11}$. A more general expression for M, than the one given in [44], is presented by Fan & Tsuchiya (1990). Eo is the ratio of the pressure of the liquid on the bubble due to gravity to the surface tension pressure. The Weber dimensionless number, We, given by

$$We = \frac{\rho_l U_b^2 d_e}{\sigma}, \qquad [56]$$

is the ratio of the liquid dynamic pressure to the surface tension pressure. The Tadaki number, Ta, is frequently used in the calculation of the aspect ratio, and the frequency of oscillation of the bubbles in their rising path. Ta is given by

Table 3. Speed and dimensionless parameters of the bubble

Bubble Trajectory	U and σ_U [mm/s]	Re_b and σ_{Re}	Eo and σ_{Eo}	We and σ_{We}	Ta and σ_{Ta}
111	193.2	526.7	0.97	1.39	1.93
	20.5	66.2	0.09	0.32	0.24
444	181.0	491.8	0.98	1.22	1.80
	20.0	61.7	0.10	0.29	0.23
555	195.7	539.4	1.00	1.45	1.98
	18.4	59.3	0.09	0.29	0.21
out	187.7	513.5	0.99	1.33	1.88
	20.4	64.3	0.09	0.31	0.24
all	190.0	519.0	0.98	1.35	1.90
	20.5	64.9	0.09	0.31	0.24

$$\mathrm{Ta} = \mathrm{Re}_b \, \mathrm{M}^{0.23}. \qquad [57]$$

A frequently used correlation to compute the aspect ratio in 3D contaminated systems is (Fan & Tsuchiya 1990)

$$\frac{h}{b} = \left[0.81 + 0.206 \tanh\left(2\left(0.8 - \log \mathrm{Ta}\right)\right)\right]^3, \qquad [58]$$

where h is the maximum vertical dimension (c). Then, the eccentricity e = 1.10, for Ta = 1.93. Thus the difference between e from [58] and $e = b / c$ from Table 2 is only between 1 to 5%. Other correlations were also used to calculate the eccentricity; they predicted shapes from spherical to ellipsoidal with e up to 1.16. This value is at most 11% higher than $e = b / c$ from Table 2. These other correlations, however, assume that there exists symmetry around the vertical axis of the bubble, and that wall influence is negligible. No information was found to compare the eccentricity for $e = b / a$. Since only average values are shown in Table 2, for the

whole range of Re_b in this experiment, the oblate spheroidal shape determined from the analysis of the images of the bubble is in agreement with Grace's and Bhaga & Weber's maps.

Table 3 shows that the inertia of the bubble is 2 orders of magnitude higher than the viscous forces, which are due to the low viscosity of the water. The pressure due to gravity is balanced by the superficial tension pressure, while the dynamic pressure of the liquid is from 30 to 40% higher than that due to the surface tension. The dominant force here is the inertia, but the system cannot be completely considered as inviscid.

Regarding the velocity of the bubbles, Table 3 shows that those bubbles traveling in trajectories close to the pipe wall are slower than those following a path in the pipe core. This is expected, because of the wall friction, which opposes to the bubble motion. The data for trajectory 555 is however unexpected. It seems that those bubbles in region 5 were actually closer to the pipe center than to the pipe wall. As with the bubble shape, the contaminants and wall affect the velocity of the bubble. The rigidness of the bubble's surface, because of contaminants present in the water, suppresses the internal circulation and decreases the rising velocity of the bubble (Clift *et al.* 1978). It also enhances vortex shedding from the boundary layer.

In an infinite medium, Grace's and Bhaga & Weber's shape maps predict $Re_b \approx 800$ for Eo = 1 and $M = 2.56\times10^{-11}$. The average values of Re_b shown in Table 3 are lower with a factor of about 30 to 40%. Observe that the errors of the velocity in Table 3 are less than 3%. The experimental data for air bubbles rising in contaminated water given by Fan & Tsuchiya (1990) and Clift *et al.* (1978) however show that Re_b is actually lower than that predicted by the maps of Grace and Bhaga & Weber. Fan & Tsuchiya show that the terminal velocity in an infinite medium $U_{T\infty}$ is about 210 mm/s for d_e = 2.7 mm, while Clift et al. give $U_{T\infty} \approx 180$ mm/s, for the same d_e and Eo = 1. Thus, Re_b = 486 from Clift *et al.*'s data, while Re_b = 567 from Fan & Tsuchiya's data. This implies that the shape maps should be considered more as qualitative representation than a reliable quantitative information source, at least in this case.

If a bubble has terminal velocity in an infinite medium $U_{T\infty}$, this will be reduced to U_T, because of wall influence according to (Clift *et al.* 1978)

$$\frac{U_T}{U_{T\infty}} = \left(1-\lambda^2\right)^{3/2}. \qquad [59]$$

In this experiment $\lambda = 0.21$, so the velocity decrease is only about 7%. The corresponding Re_b for Fan & Tsuchiya's data is 529.0, and 453.4 for Clift *et al.*'s data. In the present experiments, however, the bubbles always had a significant acceleration while crossing through the viewing volume, so terminal velocity was never reached. If, anyway, it is assumed that [59] is valid for the instantaneous velocities measured, the difference between Re_b in Table 3 and Re_b from Fan & Tsuchiya's data is less than 8%. This result shows that the tracer particles added to the water follow the data for contaminated systems, in the average results. These contaminants, however, can be responsible for the spread of the data around the mean.

Another aspect that needs consideration is that [59] is strictly valid for a fluid particle traveling along the pipe center. As shown above, bubbles rise slower as they get closer to the wall, but [59] cannot predict such velocity decrease. The data for the trajectory 444 in Table 3 shows a velocity decrease of about 7%, with respect to those for trajectory 111. In computational simulation of bubble dynamics, it is usually introduced a force to stop the bubbles from penetrating walls (Tomiyama 1998). This force, known as wall force or lubrication force, includes the diameter of the bubble, the distance to the wall and the terminal velocity. An empirical factor, the wall force coefficient, is introduced to consider different fluid systems.

6.3.2. Drag and lift forces acting on the bubble

The drag and lift forces are computed here by using the method outlined by Shridar & Katz (1995). First, note that [55] can be represented as

$$\mathbf{F_r} = \mathbf{F_i} - \mathbf{F_g} = \mathbf{F_D} + \mathbf{F_L}, \qquad [60]$$

where $\mathbf{F_i}$ is the total inertia force, and $\mathbf{F_g}$ is the buoyancy force. This equation simply shows that the drag and lift forces are balanced by the inertia and buoyancy forces. Since $\mathbf{F_D}$ is parallel to the relative velocity $\mathbf{U_r}$, it can be computed from the projection of $\mathbf{F_r}$ in the direction of $\mathbf{U_r}$. Such projection is simply the dot product between $\mathbf{F_r}$ and $\mathbf{U_r}$, that is,

$$\mathbf{F_D} = \frac{\mathbf{F_r} \bullet \mathbf{U_r}}{\|\mathbf{U_r}\|}. \qquad [61]$$

The explicit expressions for the components of F_D are given by

$$F_{Dx} = \frac{F_{rx}\,U_{rx} + F_{ry}\,U_{ry} + F_{rz}\,U_{rz}}{\|\mathbf{U}_r\|} \sin\theta\cos\varphi, \qquad [62]$$

$$F_{Dy} = \frac{F_{rx}\,U_{rx} + F_{ry}\,U_{ry} + F_{rz}\,U_{rz}}{\|\mathbf{U}_r\|} \sin\theta\sin\varphi, \qquad [63]$$

$$F_{Dz} = \frac{F_{rx}\,U_{rx} + F_{ry}\,U_{ry} + F_{rz}\,U_{rz}}{\|\mathbf{U}_r\|} \cos\theta, \qquad [64]$$

where

$$\theta = \arctan\left(\frac{\sqrt{\left(U_{rx}^2 + U_{ry}^2\right)}}{U_{rz}}\right), \qquad [65]$$

and

$$\varphi = \arctan\left(\frac{U_{ry}}{U_{rx}}\right). \qquad [66]$$

And then the lift force components can be calculated from

$$\mathbf{F}_L = \mathbf{F}_r - \mathbf{F}_D. \qquad [67]$$

Once the magnitudes of the drag and lift forces are known, the respective coefficients can be computed from their expressions given in [55], that is,

$$C_D = \frac{\|\mathbf{F}_D\|}{\frac{1}{2}\rho_l A_b \|\mathbf{U}_r\|^2}, \qquad [68]$$

and

$$C_L = \frac{\|\mathbf{F}_L\|}{\frac{1}{2}\rho_l A_b \|\mathbf{U}_r\|^2}. \qquad [69]$$

The drift and drag were computed using [60] to [67]. Then the drag and lift coefficients were calculated from [68] and [69]. The required Lagrangian velocities and accelerations were computed by tracking the bubble and tracer particles motion in three consecutive frames, as shown in figures 18 and 19. The velocity and acceleration of the liquid were interpolated to the centroid of the bubble using data from the whole test volume. These data were instantaneous measurements, that is, before the ensemble average operation used in Chapter V.

Figure 40 shows the results of the drag coefficient for all bubble trajectories as function of Re_b for two conditions. First, the full symbols present the drag coefficient under the assumption of $\mathbf{u} = \mathbf{0}$ and Ac = 0. The open symbols, on the other hand, present the drag coefficient by using [55]. In addition, Ac was included through C_M, given by [52]. Figure 40 shows an important result. The inclusion of the disturbed liquid flow field spread data. The full symbols, on the contrary, show a nice continuous trend, similar to that of the standard drag curve. This is in agreement with what was presented in the theory section, where it was stated that the flow field of the liquid should be undisturbed (on the absence of the bubble). Shridar & Katz (1995) used only liquid data from 2 to 4 d_b away from the bubble, in order to ensure that the actual undisturbed flow was used in the computations.

In this experiment all the liquid in the test volume was set in motion at the time the bubble was present, and thus it was disturbed. As just mentioned, the velocity and acceleration of the liquid used in the computations were from data of the whole test volume, including the wake. The strong oscillations of the drag coefficient in figure 40, for this case, are therefore due to the inclusion of the disturbed flow in the computations. Figures 21 to 28 show that only those regions about 2 d_b from the bubble's top can be considered undisturbed. In such regions both

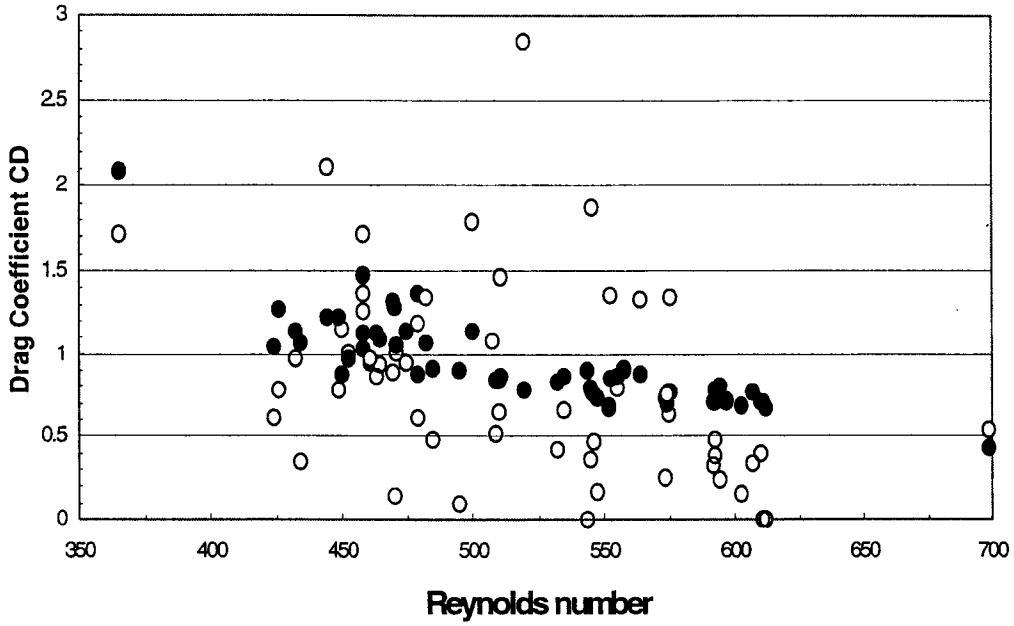

Figure 40. Drag coefficient as function of Re_b. Full symbols present data where **u** = **0** and Ac = 0 in [55]. Open symbols present data where both **u** and Ac are included in [55]. See text for explanation.

energy and vorticity are very small, so the assumption **u** = **0** is justified. In these regions the velocity magnitude is about 3 mm/s, while the acceleration has a magnitude from 100 to 300 mm/s^2. In fact, setting **u** = **0** only introduces an error to the computation of the drag and lift of about 10%. This is so because there is an order of magnitude of difference between bubble and liquid velocity and acceleration. This difference of magnitude is reflected in the magnitude of the inertia force. Of the three terms that contribute to the inertia force, the term that most contributes is the term involving C_M. This term is at least an order of magnitude higher than the other two terms, so the error introduced by neglecting the flow field velocity only affects this term. This error must be added to that due to uncertainties in the velocity and acceleration of the bubble. The total error estimation for the drag and lift coefficients is 15 to 20%, when **u** = **0** and Ac = 0.

Table 4 shows averages and standard deviations of the bubble acceleration magnitude and

Table 4. Bubble acceleration magnitude and drag coefficient

Bubble Trajectory	ac and σ_{ac} [mm/s^2]	C_{D1} and σ_{CD1}	C_{D2} and σ_{CD2}	C_D and σ_{CD}
111	2775.3	0.90	0.87	0.90
	1098.9	0.68	0.57	0.20
444	2886.7	1.04	1.00	1.07
	670.4	0.49	0.39	0.34
555	2699.2	0.47	0.57	0.86
	734.5	0.27	0.24	0.20
out	2801.5	0.78	0.80	0.98
	695.5	0.49	0.39	0.30
all	2790.5	0.83	0.83	0.94
	879.0	0.58	0.47	0.26

coefficients from 3 different computations using [55], for each bubble trajectory. The drag coefficient C_{D1} results from the inclusion of both **u** and Ac in the computations; C_{D2} includes **u**, but Ac = 0; and C_D assumes **u** = **0** and Ac = 0. Observe that Ac = 0 implies $C_M = 0.5$. The results for the drag coefficient in Table 4 again show that the inclusion of the disturbed liquid flow in the computations yields higher standard deviations, even when Ac = 0. Table 4 also shows that bubbles rising close to the wall have higher drag as a consequence of the velocity reduction, although the magnitude of the error does not allow for the quantification. The results to be presented next are those in which **u** = **0** and Ac = 0.

Figure 41 shows the drag coefficient versus the Reynolds number of the bubble computed through [68], by a widely used correlation, and assuming that the bubble reached terminal velocity. The expression of C_D at terminal velocity can be shown to be

$$C_D = \frac{4}{3}\frac{d_e}{U_b^2} g \,. \qquad [70]$$

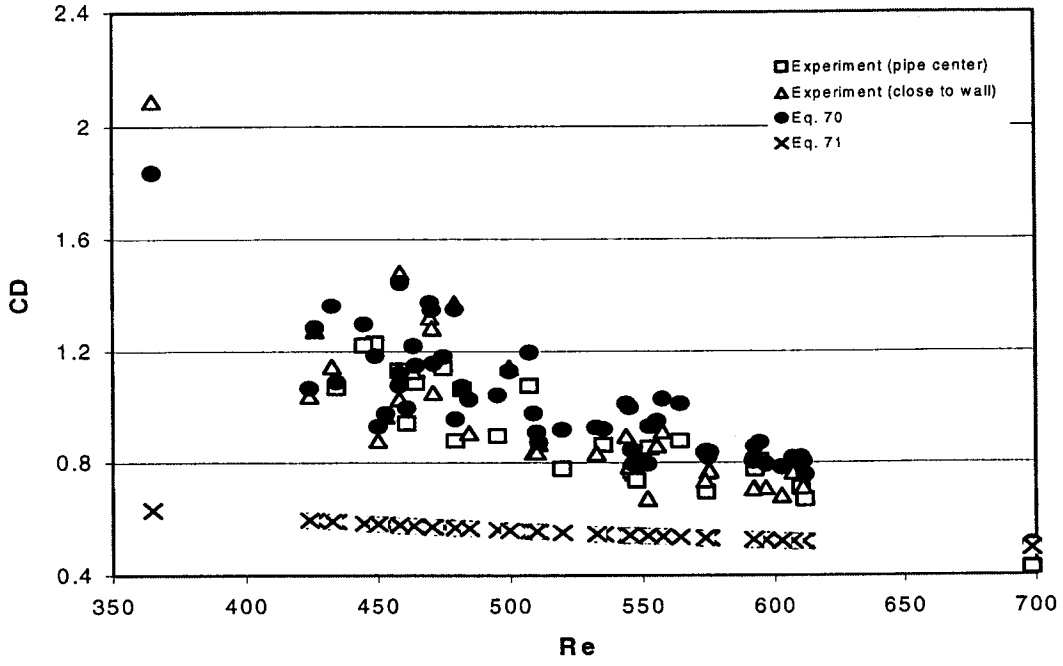

Figure 41. Drag coefficient comparison.

The terminal velocity condition implies that only the buoyancy force balances the drag. The correlation, for rigid particles but frequently used for fluid particles, between C_D and Re is given by

$$C_D = \frac{24}{\mathrm{Re}}\left(1 + 0.15\,\mathrm{Re}^{0.687}\right). \qquad [71]$$

An important result from figure 41 is that the experimental results for C_D using force balance were very close to those when C_D was calculated through [70]. In fact, the difference in the average C_D was from 5 to 10%. In all cases [70] yielded higher average values than force balance. The difference may be explained by recalling that the bubbles were not traveling at terminal velocity, so the inertia force has a contribution to the results. Another source for the difference may be due to the projected areas used in each case, because [70] assumes an

spherical particle, while in the force balance computations, the measured semiaxes were used to calculate the area. Observe, anyway, that the error associated to C_D is higher than the difference in values.

A bubble rising in spiral trajectory changes orientation. Experimentally it has been found that the frequency of orientation change is the same as that of the oscillatory motion of the bubble. The change in orientation is the angular velocity of the bubble or rotation. Bubble rotation, as explained before, induces a lateral force to the bubble, the Magnus effect. The rotation parameter R is the ratio of the angular velocity of the bubble to its translation motion, that is

$$\mathrm{R} = \frac{\sqrt{U_\alpha^2 + U_\beta^2}}{U_b}, \qquad [72]$$

where

$$U_\alpha = a\frac{\Delta\alpha}{\Delta t} \qquad [73]$$

and

$$U_\beta = b\frac{\Delta\beta}{\Delta t}. \qquad [74]$$

The change in orientation is given by $\Delta\alpha$ in the XZ plane, and $\Delta\beta$ in the YZ plane, see figures 18 and 19. Observe that there is no information available on the XY plane, so the rotation of the bubble in that plane is missing in [72].

Table 5 shows the average and standard deviation of the rotation parameter and the oscillation frequency from two equations. The oscillation frequency f is related to the Strouhal number Sr. Fan & Tsuchiya (1990) show that the f can be calculated from

Table 5. Bubble rotation parameter and oscillation frequency

Bubble Trajectory	R and σ_R	f_1 and σ_{f1} [Hz]	f_2 and σ_{f2} [Hz]
111	0.13	6.5	5.7
	0.10	0.6	1.2
444	0.22	6.6	5.6
	0.17	0.6	1.2
555	0.21	6.5	5.7
	0.15	0.6	1.2
out	0.22	6.6	5.4
	0.15	0.7	1.1
all	0.18	6.6	5.5
	0.14	0.6	1.1

$$\mathrm{Sr} = f\frac{d_e}{U_b}, \qquad [75]$$

where Sr can be computed from

$$\mathrm{Sr} = 0.100\,C_D^{0.734} \quad \text{for} \quad C_D \le 2, \qquad [76]$$

or

$$\mathrm{Sr} = 0.16\left(1.0 - \frac{0.57}{\mathrm{Ta}}\right)^2 \quad \text{for} \quad \mathrm{Ta} < 8. \qquad [77]$$

In Table 5, f_1 uses [76] and f_2 uses [77]. The average values of R clearly show that the wall

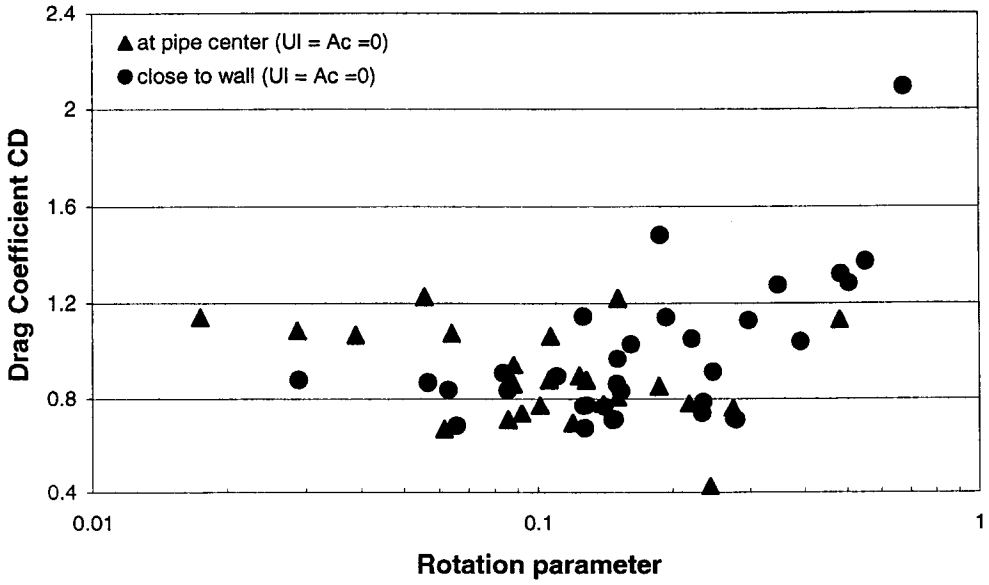

Figure 42. Drag coefficient as function of the bubble rotation parameter.

induces rotation to the bubble. The angular velocity is about 40% higher close to the wall. The average rotation can be computed using the values of R in Table 5, bubble speed in Table 3, and a and b in Table 2. Respect the oscillation frequency, f_1 is very close to the value reported for contaminated system of 7.7 Hz, for a 2 mm d_e bubble (Fan & Tsuchiya 1990). In this experiment d_e was about 2.7 mm, so it agrees with the fact that as d_e increases f decreases. The oscillation frequencies in Table 5 are for infinite mediums. Observe that a comparison with the actual oscillation frequency in this experiment is not possible, because the bubble only appears in 4 consecutive frames, which is equivalent to only 50 ms.

Figure 42 shows the influence of R in C_D. the data show no clear tendency, and simply concentrate about the mean value given in Table 4. This result is in agreement with other experimental results that showed no influence of the spinning of a particle in the drag coefficient (Crowe *et al.* 1998), although only rigid particles at high Re were used in such experiments.

Figure 43 shows the variation of the lift coefficient as function of Re, while figure 44 shows the variation respect R. There is no clear trend in the data in figures 43 and 44. Attempts to fit the data with polynomial regressions yielded regression coefficients of about 0.6. The data for

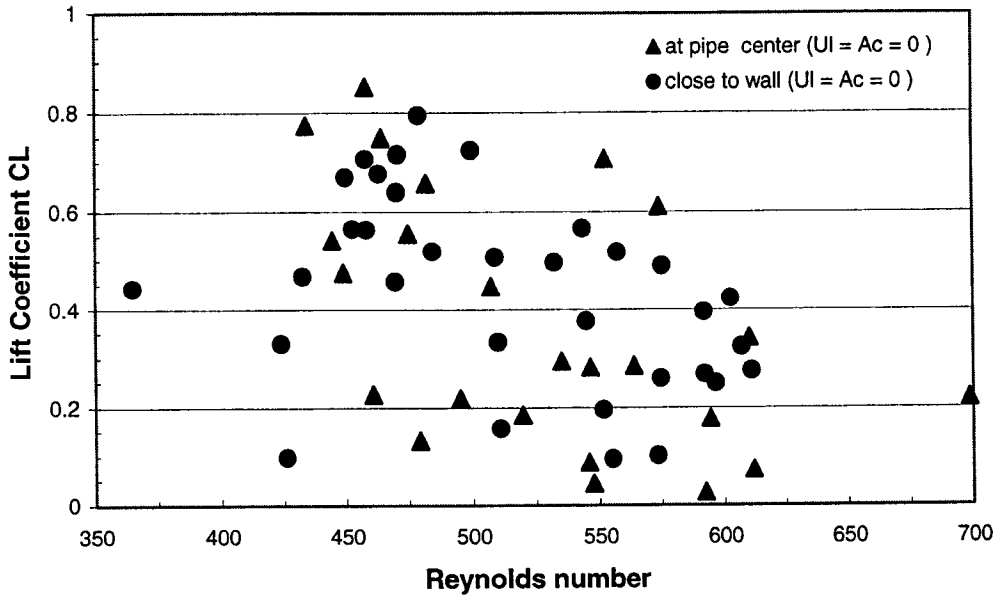

Figure 43. Lift coefficient as function of Reynolds number.

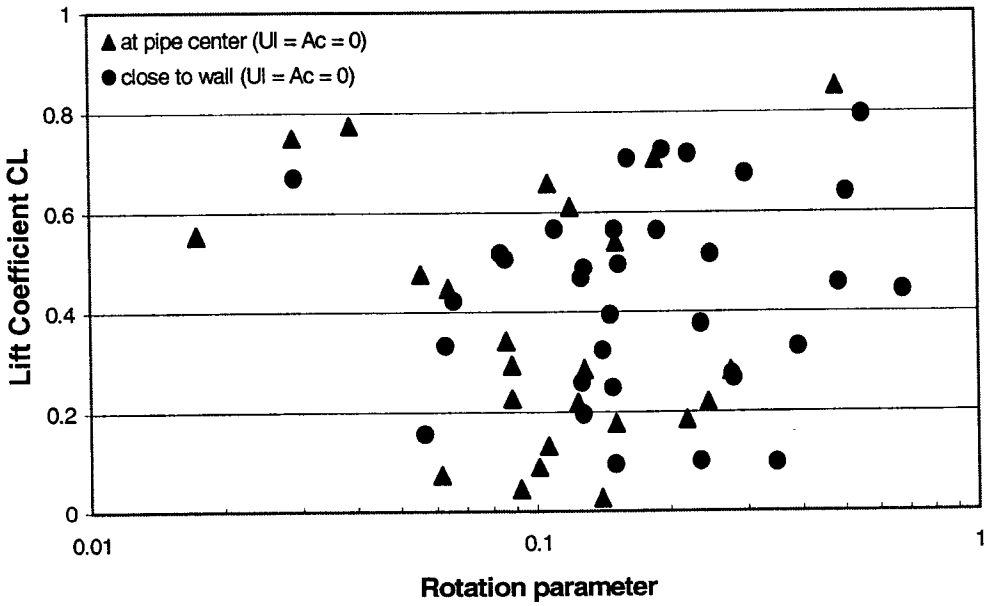

Figure 44. Lift coefficient as function of rotation parameter.

C_L is spread around 0.4. The theoretical value obtained from potential flow, and also found in some numerical studies, is 0.5. This value is for spherical particles in inviscid fluid, although it has been found to very close for ellipsoidal bubbles. The difference between the theoretical value and the present experimental results arises from the bubble shape, the wall influence, and the rocking motion of the bubble. The oblate spheroid shape indicates an asymmetry of the pressure field around the bubble. In addition, the rocking motion of the bubble implies that the bubble experience different velocity at different parts. Consequently, the pressure field changes to accommodate the velocity variations across the bubble. These pressure field variations induce lateral forces on the bubble. The lift force that an ellipsoidal bubble feels, therefore, is different than that exerted over a spherical bubble.

Observe that the measured lift force, and therefore the lift coefficient, has contributions from the Saffman and Magnus effects. The first effect comes from the shear flow generated by the flow acceleration around the bubble plus the flow deceleration because of wall friction. The Magnus force arises from the rocking motion of the bubble. The average drag force for all the bubbles rising in the trajectory in the pipe core was 9.2×10^{-5} N, while for the trajectory close to the wall the average drag force was 9.3×10^{-5} N. The lift forces were smaller, as expected. For the trajectory close to the wall, the average lift force was 4.0×10^{-5} N, while for the trajectory in the pipe center was 3.4×10^{-5} N. The average lift force is at least 40% smaller than the drag force, so the oscillatory trend of the data is directly related to the uncertainty in the measurements. Even when the measurement errors are considered, it is clear from the figures that an average value will not yield accurate predictions of the lift force.

Finally, Table 6 shows the results obtained for the average and standard deviation of the lift coefficient for three different computations. The values of the lift coefficients in Table 6 were computed in the same conditions as those in Table 4 for the drag coefficients, that is, C_{L1} was calculated similarly to C_{D1}, C_{L2} was calculated similarly to C_{D2}, and C_L was calculated similarly to C_D. The results in Table 6 again show that the introduction of the disturbed flow makes the data to oscillate around the mean values shown.

An important result in Table 6 is that the lift coefficient is higher for the bubbles rising close to the wall. Obviously, a bubble close to the wall should have experienced a higher lift force than one in the pipe core. The difference in the average values is in the range of the measurement errors, though.

Table 6. Bubble lift coefficient

Bubble Trajectory	C_{L1} and σ_{CL1}	C_{L2} and σ_{CL2}	C_L and σ_{CL}
111	0.60	0.54	0.37
	0.32	0.31	0.25
444	0.67	0.50	0.48
	0.35	0.28	0.23
555	0.66	0.45	0.38
	0.38	0.24	0.14
out	0.68	0.59	0.44
	0.37	0.34	0.20
all	0.65	0.47	0.41
	0.35	0.26	0.22